Multimessenger measurements of the static structure of shock-compressed liquid silicon at 100 GPa

H. Poole,[1,*] M. K. Ginnane,[2,3] M. Millot,[4] H. M. Bellenbaum,[5,6] G. W. Collins,[2] S. X. Hu,[2] D. Polsin,[2] R. Saha,[7] J. Topp-Mugglestone,[1] T. G. White,[7] D. A. Chapman,[8] J. R. Rygg,[2,3] S. P. Regan,[2] and G. Gregori[1]

[1]*Department of Physics, University of Oxford, Oxford OX1 3PU, United Kingdom*
[2]*Laboratory for Laser Energetics, University of Rochester, Rochester, New York 14623, USA*
[3]*Department of Mechanical Engineering, University of Rochester, Rochester, New York 14611, USA*
[4]*Lawrence Livermore National Laboratory, Livermore, California 94550, USA*
[5]*Center for Advanced Systems Understanding, D-02826 Görlitz, Germany*
[6]*Helmholtz-Zentrum Dresden-Rossendorf, D-01328 Dresden, Germany*
[7]*Department of Physics, University of Nevada, Reno, Nevada 89557, USA*
[8]*First Light Fusion Ltd., Unit 9/10 Mead Road, Oxford Pioneer Park, Yarnton, Oxford OX5 1QU, United Kingdom*

(Received 26 September 2023; revised 29 December 2023; accepted 10 April 2024; published 8 May 2024)

The ionic structure of high-pressure, high-temperature fluids is a challenging theoretical problem with applications to planetary interiors and fusion capsules. Here we report a multimessenger platform using velocimetry and *in situ* angularly and spectrally resolved x-ray scattering to measure the thermodynamic conditions and ion structure factor of materials at extreme pressures. We document the pressure, density, and temperature of shocked silicon near 100 GPa with uncertainties of 6%, 2%, and 20%, respectively. The measurements are sufficient to distinguish between and rule out some ion screening models.

DOI: 10.1103/PhysRevResearch.6.023144

With the advent of high-power lasers, a laboratory-based exploration into extreme states of matter, such as those found in planetary interiors [1] or during asteroid impacts [2], has been realized. This exotic state, referred to as warm dense matter (WDM) [3], is characterized by temperatures and pressures on the order of 1000 K and 100 GPa. Experimental measurement of material behavior and structure under such conditions is paramount for testing theoretical models used in the pursuit of fusion energy [4,5] and for modeling planetary phenomena [6–9], where dynamic geophysics processes are dominated by changes in solid- and liquid-state structure.

Over the past few decades, high-energy density (HED) facilities have generated sufficiently long-lived WDM states, enabling the deployment of advanced diagnostic suites [10–12]. Notably, the Linac Coherent Light Source's x-ray free electron laser (XFEL) has facilitated high-resolution x-ray scattering measurements for probing the electronic and atomic structure of high-pressure states [13,14]. However, XFELs face limitations in compression capabilities and achievable WDM volumes, hindering the creation of macroscopic homogeneous conditions. At kJ- to MJ-class laser facilities, conditions expected in both Jovian planet interiors [15] and fusion ignition capsules [16] can be generated. Accurately determining pressure, density, and temperature within these complex states of matter remains challenging without employing molecular-dynamics simulations in the data analysis. Furthermore, limitations in applying standard model approximations at high pressures make equation-of-state (EOS) development [17,18] costly.

Probing shock-compressed matter often relies on single diagnostics, e.g., x-ray Thomson scattering (XRTS) [19–22] or x-ray diffraction (XRD) [23–26] for measuring the electronic and atomic structures, or impedance matching techniques via a velocity interferometry system for any reflector (VISAR) [27]. Initial efforts to combine scattering and velocimetry observations to infer WDM conditions were undertaken by Falk *et al.* [28], though this required fielding each diagnostic on separate shots. These efforts highlight the critical need for platforms equipped with multiple *in situ* probing diagnostics.

In this work, an experimental platform was designed to investigate the extreme states of matter generated at high-power laser facilities. We demonstrate a crucial step forward in the endeavor to directly measure pressure, density, and temperature of WDM through a multimessenger approach. The simultaneous *in situ* structure characterization provides a unique tool for controlling diagnostic biases, measurement uncertainties, and selecting models. Reverse Monte Carlo techniques were employed to determine the shock-compressed conditions via measurement of liquid scattering [29,30]. For this study, silicon was chosen due to its importance in the understanding of planetary interiors [31,32], for its use as a dopant to ablators in inertial confinement fusion target designs [33,34], and to mitigate laser-imprint effects on multilayer targets [35,36].

The experiments were conducted at the OMEGA-EP laser facility at the Laboratory for Laser Energetics [38]. A

*hannah.poole@physics.ox.ac.uk

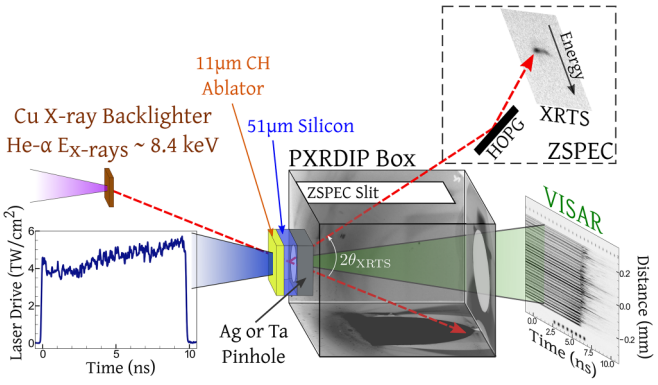

FIG. 1. Experimental setup at the OMEGA-EP laser facility. The silicon target is mounted on the front of the PXRDIP box [37] with a 100-μm-thick, 0.5-mm-diam Ag or Ta pinhole. A single beam drives the CH-Si target with a tailored pulse as shown in the inset. The remaining three lasers generate Cu He-α x-rays. The red dashed lines represent the scattered x-ray paths that are collected by the XRTS and XRD IPs. The raw data shown were collected from s30967. NB: Not drawn to scale.

51-μm-thick polycrystalline silicon sample was shock-compressed to ∼100 GPa using a single drive laser beam delivering ∼440 J over 10 ns with an ∼1.1-mm-diam distributed phase plate. The drive laser was incident on a 11 μm polystyrene (C_8H_8) ablator at a 19.3° angle with respect to the target normal. The ablator was fixed to the front of the silicon sample using a thin layer of glue (<1 μm). Three additional beams were tightly focused on a 12.5-μm-thick copper backlighter with an areal size of 4 mm^2, generating a 1 ns pulse of Cu He-α x-rays centered at $E \sim 8.4$ keV [39]. The x-ray source was placed ∼17 mm away from the silicon sample.

The experimental configuration devised to probe the structure of WDM silicon at OMEGA-EP is shown in Fig. 1. It employed a variation of the powder x-ray diffraction image plate (PXRDIP) setup [26], which uses Fujifilm BAS-MS image plates (IPs) [40]. Due to spatial constraints, the x-ray diffraction only accessed momentum transfers up to $k \sim 4$ Å^{-1} at 8.4 keV. To extend the capabilities of the PXRDIP diagnostic, OMEGA's Bragg crystal spectrometer (ZSPEC) was added to measure scattering at high momentum transfer, and it is capable of resolving the electronic structure of sufficiently ionized systems. The ZSPEC consists of a 25 mm × 50 mm highly oriented pyrolytic graphite (HOPG) crystal with a radius of curvature of 27 mm, and placed 12.8 cm after the sample. As shown in the top inset in Fig. 1, the ZSPEC was fielded out of perfect von-Hamos focusing, meaning the x-rays were spectrally dispersed on a curve. The silicon sample was fitted to the front of the PXRDIP enclosure on top of a 0.5-mm-diam silver or tantalum collimating aperture pinhole, which restricts the diagnostics' line-of-sight to the central planar shock region. These materials were chosen to ensure no fluorescence within the ZSPEC energy range, and to reduce interference between the pinhole and silicon Bragg peaks on the PXRDIP.

To measure the shock-breakout (SBO) time, we fielded line-imaging VISAR, which monitored the silicon sample's free surface [41]. The streaked image inset in Fig. 1 shows the SBO as a rapid disappearance of the fringes around ∼5 ns. As silicon is opaque to the VISAR wavelength (532 nm) at the investigated conditions, direct measurements of shock and particle velocity are only achievable by employing witnesses and pressure windows. However, introducing these materials is unsuitable for scattering measurements due to the significant resultant contamination, making it difficult to isolate the scattering signal from the liquid silicon. Instead, utilizing the bilinear relationship in Ref. [27], which for small velocities is calculated from previous high explosive measurements [42], the silicon shock velocity is determined as 9.5 ± 0.2 km/s. As detailed in Appendix C, combining this shock velocity with the Rankine-Hugoniot relations, we measured the achieved pressure-density state to be 101 ± 6 GPa and 4.43 ± 0.08 g/cm^3.

At these conditions, silicon is expected to be in the fluid state, which occurs when dynamically compressed above 30 GPa [14,43]. While liquid silicon scattering, up to 30 GPa, has been previously observed at XFELs [14], extracting the contribution from low-Z liquids at high-power laser facilities is experimentally challenging due to limited x-ray source brightness, the presence of fluorescence, spurious scattering from the pinhole, and x-ray emission in the drive ablation plasma. To achieve this, we quantified the contribution from the pinhole, ablation plasma, and ambient sample. The procedure is described in detail in Appendix B.

As shown in Fig. 2(a), a broad scattering feature, attributed to liquid silicon, is observed around $2\theta \sim 45°$. Due to the PXRDIP's geometry and the broadband x-ray emission from the laser-generated plasma plume, shadows from the box appear on the IPs, preventing a complete azimuthal integration in ϕ-space. Instead, a partial integration is performed by selecting regions with reduced contamination from the aforementioned sources. The resultant signal for a reference shot (s30970), which contained only the pinhole and ablator, and a driven silicon sample (s30967) are shown in Fig. 2(b) in green and blue, respectively. The final liquid silicon scattering signal, $I_{liq}(k)$, shown in Fig. 3(a) is obtained by subtracting the reference shot from the driven sample, and excluding the 2θ regions around the pinhole Bragg peaks. Further details can be found in Appendix B. A 2θ error of ∼0.5° is taken to be the average deviation of the observed pinhole Bragg peaks from their expected values.

Additionally, the fraction of shocked (fluid) material within the probe volume was inferred using the ZSPEC diagnostic by comparing data obtained with varying time delays between the drive laser and x-ray probe. As the volume of liquid silicon increases, the elastic scattering signal recorded on the XRTS, fielded in-between Bragg peaks, becomes more intense. From the elastic signal measured on s30967, the volume fraction was found to be ∼0.6 (see Appendix A for the full spectral analysis). Due to the low ionization of the liquid silicon, an inelastic scattering feature was not resolved above the ZSPEC instrumental noise.

At high momentum transfers, the liquid scattering signal is the result of coherent, $I_{coh}(k)$, incoherent, $I_{incoh}(k)$, and multiple, $I_m(k)$, scattering. As the silicon thickness is small relative to its attenuation length, $I_m(k)$ is assumed to be negligible. The experimentally measured $I_{liq}(k)$ is related to the normalized

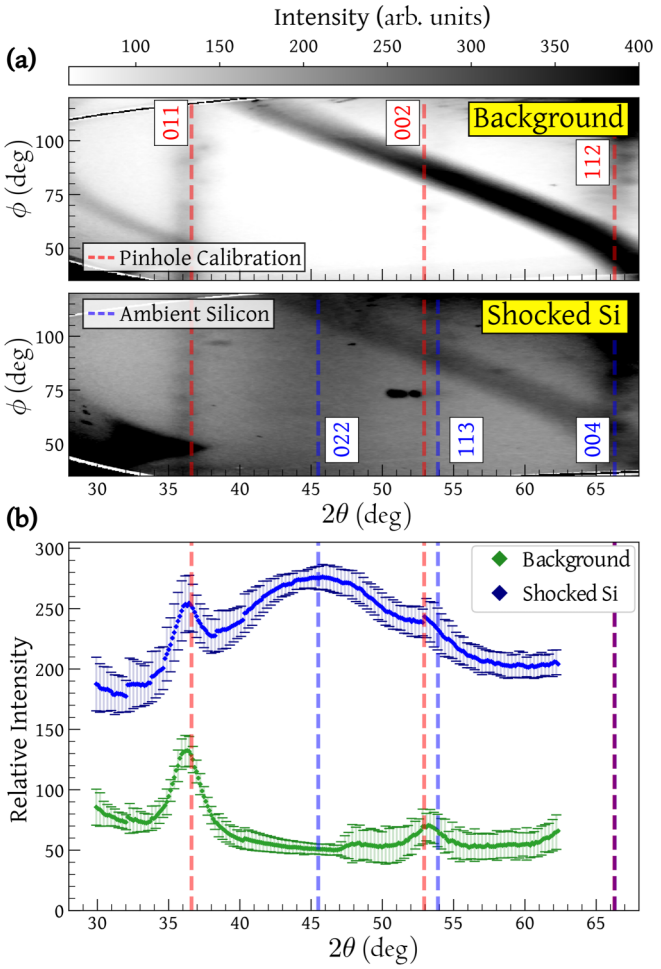

FIG. 2. (a) X-ray diffraction data, projected into 2θ-ϕ space [37], from background shot s30970, where no Si was placed in the target holder, and the liquid Si diffraction from s30967. The superimposed red and blue dashed vertical lines are the expected 2θ Bragg diffraction peaks of the Ta pinhole and ambient silicon, respectively. (b) Relative intensities of the partial-ϕ integrated scattering shown for the background (in green) and shock-compressed silicon (in blue) shots.

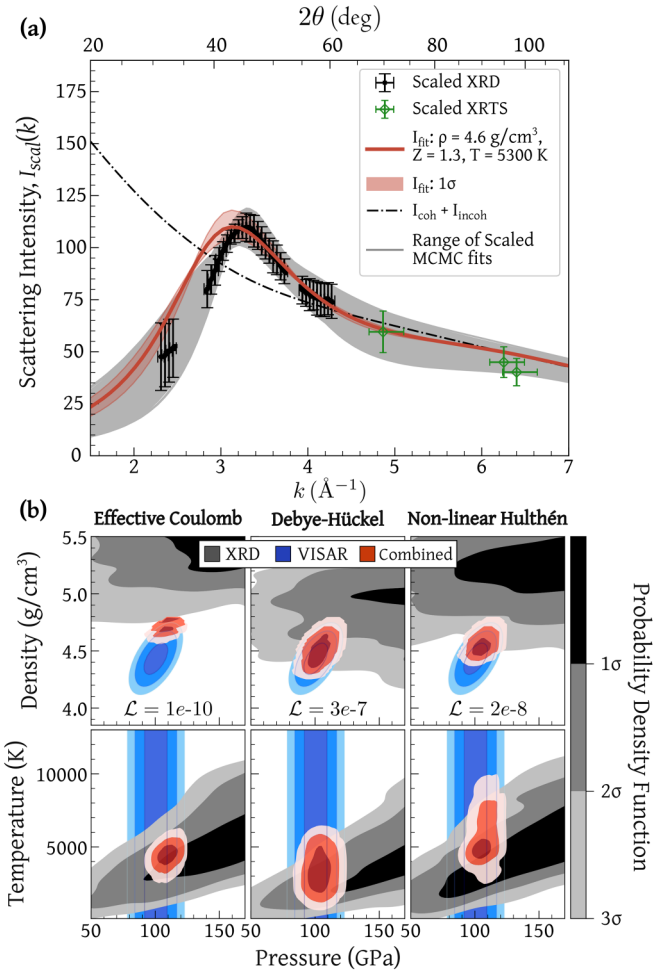

FIG. 3. (a) Liquid Si diffraction signal, $I_{\rm scal}(k)$ (in black), is shown scaled to the theoretical signal, $I_{\rm fit}(k)$ (thick red line), produced by the combined VISAR and converged MCMC conditions using the nonlinear Hulthén model. The 1σ error of $I_{\rm fit}(k)$ is shaded in red. The dash-dotted black line shows $I_{\rm coh} + I_{\rm incoh}$ for these values. The broad range of accepted MCMC fits (in gray) are scaled to the mean fit. (b) Probability density functions in the P-ρ and P-T phase for VISAR (blue heat maps) and x-ray scattering (gray heat maps) analysis using each V_{ii}. The corresponding joint distributions are superimposed as red heat maps. In the upper grid, the likelihood, as defined in Eq. (3), of each V_{ii} is shown.

ion-ion structure factor, $S_{ii}(k)$, via [44,45]

$$\frac{I_{\rm liq}(k)}{\gamma} \equiv I_{\rm scal}(k) = I_{\rm coh}(k)[S_{ii}(k) - 1] + [I_{\rm coh}(k) + I_{\rm incoh}(k)], \tag{1}$$

where $I_{\rm coh}(k) = |f(k) + q(k)|^2$, with $f(k)$ the form factor of the tightly bound electrons and $q(k)$ that of the free electrons that follow the ion motion [46]. The factor γ is a scaling constant defined such that $I_{\rm scal}(k \to \infty) = I_{\rm coh}(k) + I_{\rm incoh}(k)$. To be experimentally obtained, momentum transfers in excess of 10 Å^{-1} are required, a regime not currently accessible at high-power laser facilities. Here, $I_{\rm incoh}(k)$ is obtained using the tabulated values from Ref. [47], and $I_{\rm coh}(k)$ is simulated using the multicomponent scattering spectra (MCSS) code [48]. As detailed further in Appendix E, γ is left proportional to a free random Gaussian scalar with a standard deviation equal to the noise of the raw data.

The large parameter space, $\Psi(\rho, T, Z)$, is explored using a Markov-Chain Monte Carlo (MCMC) procedure [30,49]. This uses Bayesian inference to determine the likelihood of a set of parameters producing the experimental spectrum based on an acceptance percentage $P[I_{\rm scal}(k)|\Psi] = {\rm e}^{-\beta_{\rm cost}}$ with

$$\beta_{\rm cost} = \max\left[\frac{I_{\rm fit}(k) - I_{\rm scal}(k)}{\sqrt{2}\sigma\,\Sigma}\right]^2, \tag{2}$$

where Σ is the error on $I_{\rm scal}$, and $\sigma = 0.5$ is a scalar chosen to allow acceptance freedom within data uncertainty. The investigated parameter space assumed a uniform distribution with linear sampling for the density, $2.33 \leqslant \rho\,({\rm g/cm^3}) \leqslant 6$, ionization, $0 \leqslant Z \leqslant 14$, and temperature, $10^3 \leqslant T_e = T_i\,({\rm K}) \leqslant 1.1 \times 10^4$.

Simulating $S_{ii}(k)$, however, is subject to model biases and requires appropriate selection of electron and ion interactions. Measurement of the liquid structure factor opens the opportunity for direct model comparison. In the partially ionized, low-density state, the ion-ion interaction potential, $V_{\rm ii}(k)$, is commonly modeled using Debye-Hückel (DH) [50]. This work compares the DH model with the bare (unscreened) effective Coulomb (EC) interaction and a model nonlinear Hulthén (NH) interaction [51]; the latter approximately describes screening beyond the DH approach. For the screening cloud, $q(k)$, large momentum transfers in high-density matter have shown deviation from the simple DH model as a result of finite-wavelength screening (FWS) [52]. As detailed in Appendix E, the simulated liquid scattering is comparatively insensitive to each $q(k)$ model, and FWS was chosen for the MCMC analysis.

In Fig. 3(a) the range of accepted fits after MCMC convergence using the NH model are shown in gray. The signal from the XRTS recorded on shots that were probed after shock breakout (where the liquid volume fraction >0.9) is compared in green against the angularly resolved scattering in Fig. 3(a), extending the effective k range. While these points were not included in the MCMC fitting process due to the lack of an absolute signal intensity calibration between XRD and XRTS, they nonetheless exhibit good agreement with the results.

Using a suitable theoretical description, the plasma pressure can be determined from the range of accepted fits. Under conditions of strongly coupled ions and degenerate electrons, where screening is expected to be significant, a reasonable framework is the "two-fluid" model discussed by Vorberger *et al.* [53,54] (see Appendix E). The converged probability density functions $\Pr(P, \rho)$ and $\Pr(P, T)$, for each V_{ii}, are shown in gray in Fig. 3(b) and compared, in blue, to the P-ρ state inferred using VISAR. Combining these concurrent diagnostics, we find the joint P-ρ probability density functions, superimposed in Fig. 3(b) as red heat maps.

The likelihood of each V_{ii} model given the VISAR information is defined as the sum of its joint probability distribution,

$$\mathcal{L}(V_{ii}|\text{VISAR}) = \sum_{\rho,P} \Pr_m(P, \rho) \times \Pr_v(P, \rho)\,, \qquad (3)$$

where m and v denote the MCMC and VISAR probability density functions, respectively. These likelihoods are indicated in the upper grid of Fig. 3(b). They show that comparatively, the effective-Coulomb model is a poor representation of the liquid silicon state. This is expected as it does not account for screening effects.

The limited observed overlap between the VISAR and XRD probability distribution functions (PDFs) can be attributed to various factors. First, each diagnostic is sensitive to distinct aspects of the shock-compressed conditions, leading to differences in their observed distributions. Moreover, it is worth noting that the VISAR Hugoniot measurement is derived from data collected in Ref. [42] where no experimental uncertainty was provided. Consequently, this results in a narrower uncertainty on the VISAR PDF. However, this constraint may be refined should more experimental silicon Hugoniot information in this regime become available, or if advancements are made in experimental platforms that allow for the inclusion of witnesses and pressure windows without contaminating the observed liquid scattering. Secondly, the relative simplicity of the screening models investigated in the x-ray scattering data implies that they are not absolute representations of the underlying physics. While more refined models may be attainable through the utilization of density function theory (DFT) simulations [55,56], such methodologies are computationally expensive and introduce varying degrees of complexity in the models.

Despite these uncertainties, there are parameter spaces common to both diagnostics. By combining their PDFs, we can achieve a more comprehensive understanding of the shock-compressed conditions by constraining the XRD parameter search to those consistent with the pressure-density Hugoniot relation established by the VISAR measurement. Furthermore, a discernible difference in the condi-

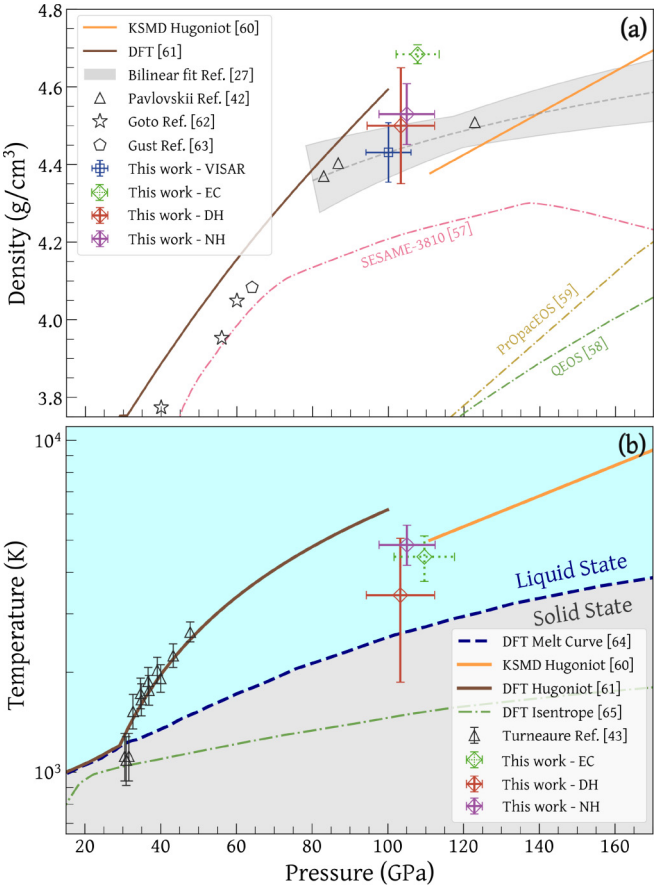

FIG. 4. (a) The principal silicon Hugoniot where this work is compared to SESAME-3810 [57], quotidian equation-of-state (QEOS) [58], PrOpacEOS [59], *ab initio* Kohn-Sham DFT molecular-dynamics (KSMD) [60], principle Hugoniot from DFT [61], and previous experimental work collected via conservation methods [42,62,63]. The bilinear fit [27] used to infer particle velocity is shown as a filled gray bar. (b) The silicon pressure-temperature phase diagram comparing the combined 1σ error for each $V_{\rm ii}$ to the measured and predicted melt curve [64], the DFT isentrope [65], and previous shocked silicon experiments [43] where the temperature was inferred using molecular dynamics [66].

tions inferred utilizing each screening model can still be observed.

Unlike the VISAR diagnostic, the MCMC convergence of the x-ray scattering analysis is dependent not only on pressure and density, but also on temperature. Propagating the combined $\Pr(P, \rho)$ into temperature space redistributes the x-ray scattering $\Pr(P, \rho, T)$ to penalize where the density and pressure disagree with VISAR (see Appendix F for further details). The resultant $\Pr(P, \rho, T)$ are used to find the combined 1σ errors in the pressure-temperature phase, shown in red in the lower grid of Fig. 3(b). The simulated x-ray diffraction fits, I_{fit}, produced by the conditions inferred when combining VISAR and the NH MCMC convergence are shown in red in Fig. 3(a).

In Fig. 4 the VISAR and MCMC combined 1σ P-ρ and P-T for each V_{ii} model are plotted on the principal Hugoniot. Despite having the closest agreement with VISAR in P-ρ, the temperature predicted by the Debye-Hückel model falls below the Hugoniot state. Instead we find that the implementation of a Hulthén potential [51], which estimates nonlinear screening regimes beyond DH, better describes the thermodynamic conditions. This platform, therefore, demonstrates the capability to effectively distinguish between screening models, which is essential for accurately predicting material behavior under extreme conditions.

This paper presents detailed insights into the extreme states of matter generated at high-power laser facilities. While previous studies on liquid silicon have been confined to pressures around ∼50 GPa [14,43], the combination of multiple *in situ* diagnostics, along with MCMC analysis, effectively reduces diagnostic biases and yielded uncertainties on the shock-compressed state that are comparable to previous experimental work, without relying on EOS models. Furthermore, the synergistic combination of diagnostics facilitated the differentiation of distinct static screening models. The results revealed the necessity of incorporating screening beyond the linear Debye-Hückel approach, employing a Hulthén potential, to achieve agreement between the measured liquid silicon state and Hugoniot predictions. Therefore, this platform paves the way for exploring the structure of HED matter at high-power laser facilities.

ACKNOWLEDGMENTS

This material is based upon work supported by the Department of Energy National Nuclear Security Administration under Award No. DE-NA0003856, the University of Rochester, and the New York State Energy Research and Development Authority and the National Science Foundation under Grant No. PHY-2045718. Part of this work was prepared by LLNL under Contract No. DE-AC52–07NA27344. The PXRDIP data were analyzed with LLNL AnalyzePXRDIP package. This work was partially supported by the Center for Advanced Systems Understanding (CASUS), financed by Germany's Federal Ministry of Education and Research (BMBF) and the Saxon state government out of the State budget approved by the Saxon State Parliament. This work has received funding from the European Union's Just Transition Fund (JTF) within the project Röntgenlaser-Optimierung der Laserfusion (ROLF), Contract No. 5086999001, cofinanced by the Saxon state government out of the State budget approved by the Saxon State Parliament.

This paper was prepared as an account of work sponsored by an agency of the U.S. Government. Neither the U.S. Government nor any agency thereof, nor any of their employees, makes any warranty, express or implied, or assumes any legal liability or responsibility for the accuracy, completeness, or usefulness of any information, apparatus, product, or process disclosed, or represents that its use would not infringe privately owned rights. Reference herein to any specific commercial product, process, or service by trade name, trademark, manufacturer, or otherwise does not necessarily constitute or imply its endorsement, recommendation, or favoring by the U.S. Government or any agency thereof. The views and opinions of the authors expressed herein do not necessarily state or reflect those of the U.S. Government or any agency thereof.

APPENDIX A: SPECTRALLY RESOLVED X-RAY SCATTERING

The zinc-spectrometer (ZSPEC) diagnostic used to record the x-ray Thomson scattering consisted of a highly oriented pyrolytic graphite (HOPG) crystal placed 12.8 cm after the sample. The central Bragg angle was 13.2° with an angular spread of 2.5°. Its image plate (IP) was protected by a 5 mm Be filter and mounted 13.1 cm from the crystal meaning the ZSPEC was fielded out of perfect von-Hamos focusing. This resulted in the spectrally resolved x-rays being scattered onto a cone, which can allow for some spatial information to be resolved. In the raw intensity image shown in Fig. 5(a), the x-ray scattering cone is highlighted in black and the scattered photon energy increases to its point. The dispersion of the ZSPEC is [67] $\Delta E/\Delta x \sim 7\,\text{eV/pixel}$ where the pixels are 50 μm wide. To extract the spectrally resolved spectrum, the total scattering signal along each energy arc is determined. The pixels falling along an arc, such as those highlighted in red, have an average pixel background value (determined from the orange arcs which fall outside of the x-ray scattering cone) removed, and they are then summed. This gives an integrated scattering signal, $I(x)$, for a given spatial position x on the IP. The spectrum is converted from spatial to energy space using

$$\begin{aligned} I(E) &= \frac{hc}{2d}\csc\left[\tan^{-1}\left(\frac{I(x) + D_c\sin\theta_0 + D_{ip}\sin\theta_0}{D_{ip}\cos\theta_0 + D_c\cos\theta_0}\right)\right] \\ &\equiv \frac{hc}{2d}\csc(\tan^{-1}(\psi)) \\ &= \frac{hc}{2d}\sqrt{1+\frac{1}{\psi^2}}\,, \end{aligned} \tag{A1}$$

where $2d = 0.67\,\text{nm}$ is the HOPG lattice spacing, $D_c = 12.8\,\text{cm}$ is the distance from the source to the HOPG crystal, $D_{\text{ip}} = 13.1\,\text{cm}$ is the distance from the HOPG crystal to the IP, and $\theta_0 = 13.2°$ is the central Bragg angle on the crystal. In the upper plot of Fig. 5(b), the XRTS spectrum from the Cu x-ray source is shown. After a further polynomial fit to the background is removed, the total background removed spectrally resolved XRTS spectrum is given in the lower plot of Fig. 5(b). The energy calibration is performed by

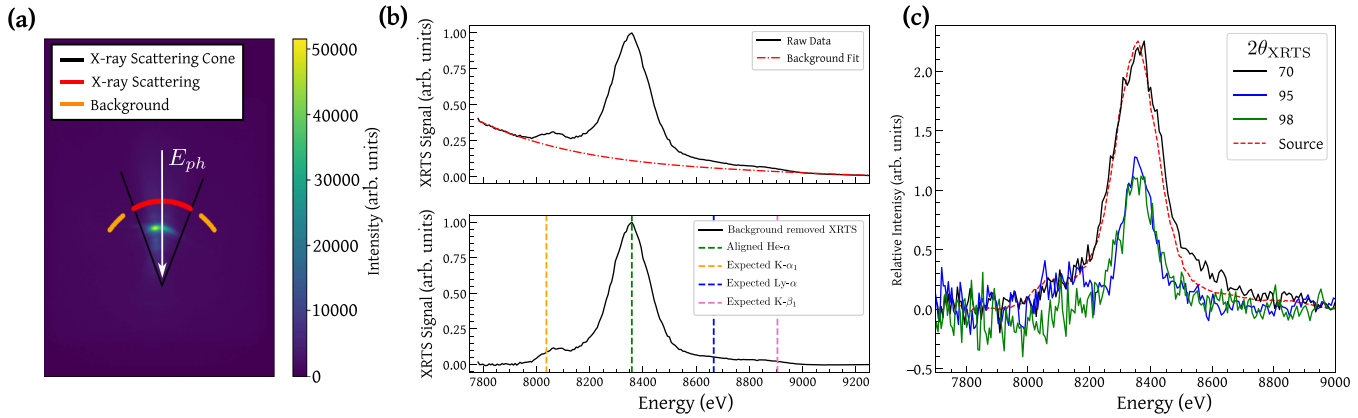

FIG. 5. (a) Raw intensity of calibration s33544 where the Cu foil was placed in the target holder of the PXRDIP box. (b) In the top plot, the XRTS spectrum extracted after integrating along each energy arc is shown. A further polynomial background fit (red dash-dotted line) is subtracted from the overall signal to produce the spectrum in the lower plot. The energy axis is calibrated to the Cu He-α peak. The expected positions of the remaining Cu transitions are shown as vertical dashed lines. (c) Comparison of the spectrally resolved XRTS signal for the post-SBO shots where $V_l/V_s > 0.9$. The source function from (b) is scaled to the $\theta_{XRTS} = 70^\circ$ scattering signal and is shown as a red dashed line.

aligning the peak signal with the Cu helium-α x-ray transition at 8.358 keV. It can be seen in the lower plot that the remaining expected Cu transitions align with the lower intensity peaks observed on the spectrum.

A comparison of the XRTS spectra produced by the data shots taken after SBO (i.e., where $V_l/V_s > 0.9$) is shown in Fig. 5(c) against the source function. As expected with low silicon ionization, there is no resolvable inelastic scattering signal above the source function. The XRTS signals, therefore, cannot be used independently to extract the plasma parameters, but they can be combined with the x-ray diffraction.

To compare the XRTS to the angularly resolved x-ray diffraction signal, the XRTS must be spectrally integrated to give $I(k) = \sum_\omega I(k, \omega)$. However, as only the coherent scattering signal is clearly observed over the background noise, an integration over all ω-space cannot be performed. Additionally, using the peak intensity of the spectrally resolved signals shown in Fig. 5(c) as a measurement of their relative coherent scattering signal, L_{coh}, would introduce significant uncertainty due to the compounded error of isolating the x-ray scattering cone and from the integration methods performed over each energy arc. Instead, as demonstrated in Fig. 6, their L_{coh} are determined by removing fitted background Gaussian distributions from the overall signal intensities—isolating the target scattering. The signals are corrected for filtering, polarization, backlighter distance, and relative thickness of the silicon seen by the x-ray source. The subsequent Gaussian fits to these scattering histograms yield $L_{coh} = (\mu_s + 2\,\sigma_s) - \mu_b$, where s and b denote the Gaussian distributions to the scattering and background signals, respectively. The coherent scattering intensities are listed in Table I.

For the ambient s30968, where $2\theta_{XRTS} = 70^\circ$, the Ta Bragg peak from the (112) lattice plane is resolved by the XRTS. This pinhole scattering signal is isolated from the silicon scattering by subtracting the XRTS coherent signal from the reference s30970, where only the Ta pinhole was loaded in the target holder. As discussed in the main paper, comparing the coherent scattering intensities of ambient and shocked silicon provided information on the fraction of shocked (fluid) silicon within the probe volume. Using a simple scattering model as described by Pelka *et al.* [68], which is based on the approach of Chihara [46], the time-averaged volume fraction of liquid (l) to solid (s) silicon present during the scattering event is calculated as

$$\frac{V_l}{V_s} = \frac{L^l_{coh}}{L^s_{coh}} \frac{S^s_{tot}}{S^l_{tot}} = \frac{L^l_{coh}}{L^s_{coh}} \frac{Z_{Si}\left[1 - I_{coh}(k)/Z^2_{Si}\right]}{I_{coh}(k) S_{ii}(k)}, \tag{A2}$$

where S_{tot} are the static structure factors and $Z_{Si} = 14$ is the nuclear charge. As shown in Fig. 6, the volume fraction for the shock-compressed silicon states was found to be $V_l/V_s > 0.6$.

As shown in Fig. 3(a), the postshock breakout XRTS data shots (s30964, s33538, and s33541)—where the fraction of liquid silicon is greater than ~0.9—are compared to the diffuse angularly resolved scattering recorded on s30967. These L_{coh} signals are scaled by fitting the value at $2\theta_{XRTS} = 70^\circ$ to the range of accepted MCMC fits. As only the coherent contribution is resolved using ZSPEC, this fitting procedure uses the MCMC fits, I_{fit}, prior to adding the incoherent scattering, I_{incoh}. The higher $2\theta_{XRTS}$ signals are then determined by their scattering intensity relative to the 70° data. The total signal errors are compounded by their respective coherent scattering uncertainties and the scaling error of L_{coh} at 70°.

APPENDIX B: ANGULARLY RESOLVED X-RAY SCATTERING

Using Lawrence Livermore National Laboratory's AnalyzePXRDIP procedure [37], the raw x-ray diffraction IPs, shown in Figs. 7(a) and 7(b), are warped into 2θ-ϕ by using the Ta pinhole Bragg peaks as calibrants. The pinhole calibration for each shot is shown in (c) and (d). To isolate the liquid silicon scattering, the background signal must be removed from the shocked data. While a variant of the statistics-sensitive nonlinear iterative peak-clipping (SNIP) algorithm is often used to isolate the signal from the background in PXRDIP scattering data [37], this process is only appropriate when dealing with sharp Bragg peaks, such as

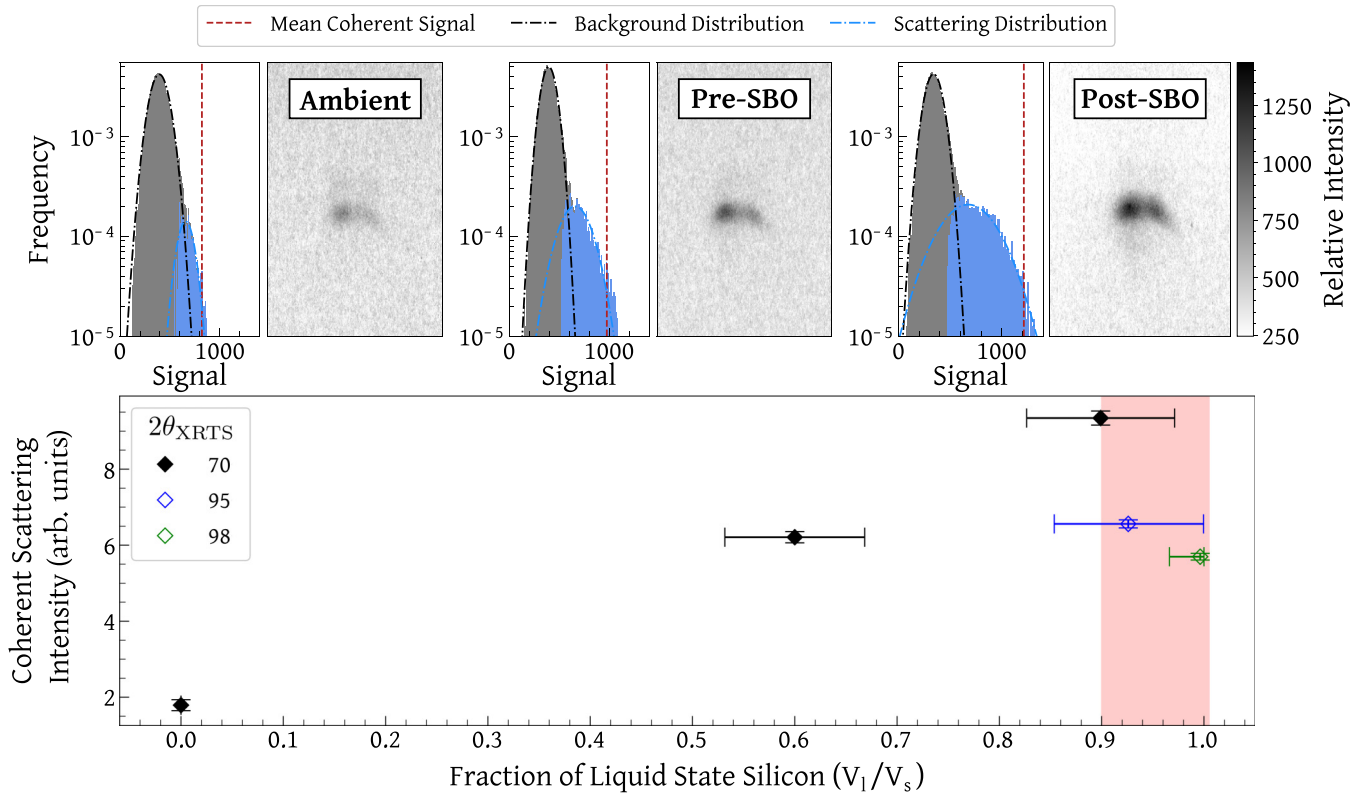

FIG. 6. The XRTS signal intensities focused around the coherent scattering arc for ambient s30968 (a), pre-SBO s30967 (b), and post-SBO s33538 (c) at $2\theta_{XRTS} = 70°$. The raw scattering image is shown on the right of each plot, and their corresponding scattering signal histograms are shown on the left. The red dashed lines are the mean coherent signal intensities, L_{coh}. **(d)** Relative intensity of the elastic XRTS signal ($\propto S_{ii}$) against the fraction of liquid silicon, V_l/V_s, for all $2\theta_{XRTS}$. Highlighted in red are the shots taken after shock-breakout. For these shots, the liquid fraction is greater than ~0.9 and the scattering is assumed to be only from liquid silicon. The liquid fractions of the unfilled diamond points at 95° and 98° are determined from HELIOS simulations due to insufficient ambient data at these scattering locations.

shown in Fig. 7. As discussed in the main paper, to quantify the background signal we instead performed a series of shots to isolate each contributor. In s30966, as shown in Fig. 8(a), we investigated the signal intensity recorded on the IPs when only the drive laser was present (i.e., no x-ray probe). At the investigated pressure, this was found to be negligible in comparison to the data collected with x-ray scattering events. In addition, the signal contamination from the addition of the ZSPEC access slit in the PXRDIP box was investigated in s33539, shown in Fig. 8(b). The only contamination region was found to be around the access slit. This region was therefore excluded in future analysis. Comparison of the scattering recorded on the PXRDIP using an ambient silicon sample (e.g., s30968) versus for a reference s30970, where the silicon sample was removed, showed the dominant background scattering contributor to be the pinhole.

TABLE I. Experimental parameters for all shots including the total incident energy of the shock-compression drive, E_{drive}, and x-ray, E_{xray}, lasers.

Shot	$2\theta_{XRTS}$ (deg)	Pinhole	h_{CH} (μm)	h_{Si} (μm)	E_{drive} (J)	E_{xray} (J)	t_{drive} (ns)	t_{xray} (ns)	t_{SBO} (ns)	L_{coh}
Background target–No silicon										
30970	70	Ta	11 ± 2			3760.7				260 ± 9
Ambient conditions										
30968	70	Ta	11 ± 2	51 ± 1		3618.6				430 ± 10
Shock-compressed conditions										
30964	95	Ta	11 ± 2	51 ± 1	441.3	3707.5	-0.049 ± 0.025	5	5.35 ± 0.04	615 ± 10
30967	70	Ta	11 ± 2	51 ± 1	429.0	3908.4	-0.15 ± 0.025	4.8	6.22 ± 0.06	580 ± 10
33538	70	Ag	11 ± 2	51 ± 1	437.9	3778.3	-0.002 ± 0.025	5	5.20 ± 0.04	875 ± 20
33541	98	Ag	11 ± 2	51 ± 1	422.5	3835.0	0.014 ± 0.025	5	4.91 ± 0.03	534 ± 8

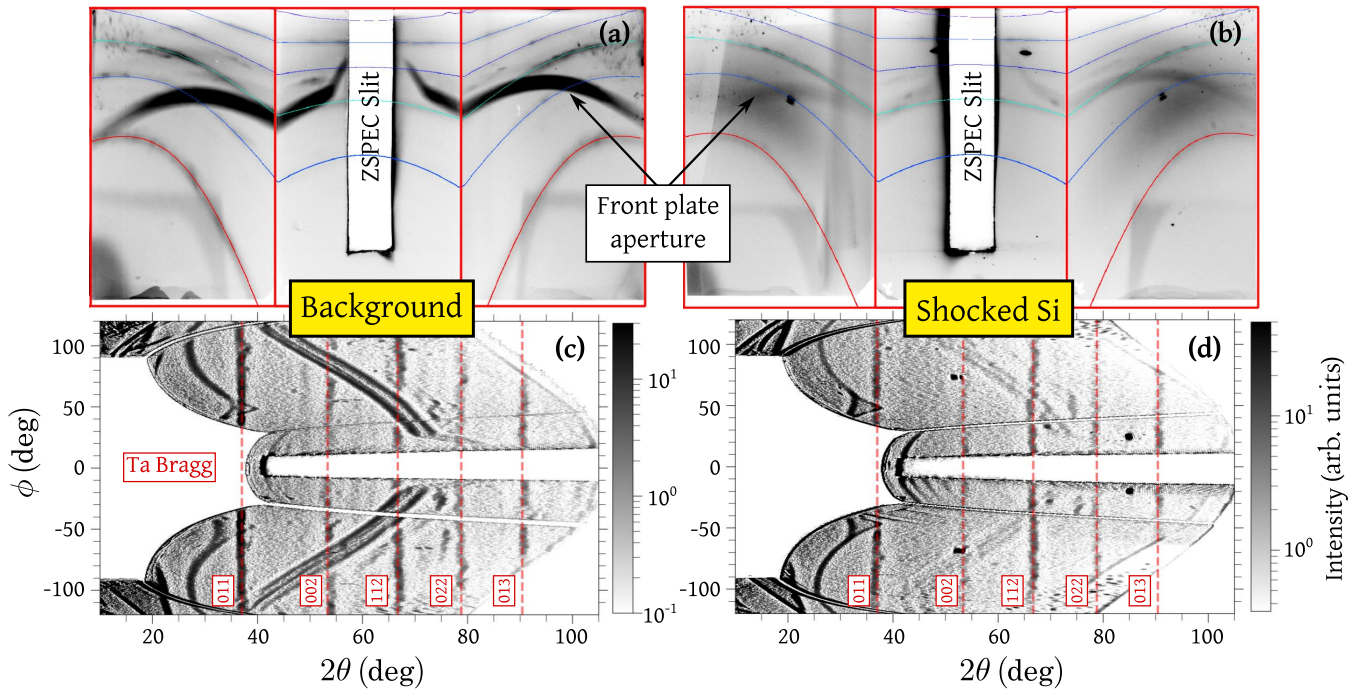

FIG. 7. (a) and (b) Raw image plates for background s30970 and shocked silicon s30967, respectively. The lines shown are the Bragg diffraction peaks of the Ta pinhole, which are used to calibrate the geometry of the PXRDIP box. Their corresponding warped 2θ-ϕ signals at the pinhole position are shown in (c) and (d), respectively. The scattering distributions for the pinhole used a SNIP background removal process [37] which enhances sharp peaks, improving signal-to-background ratios.

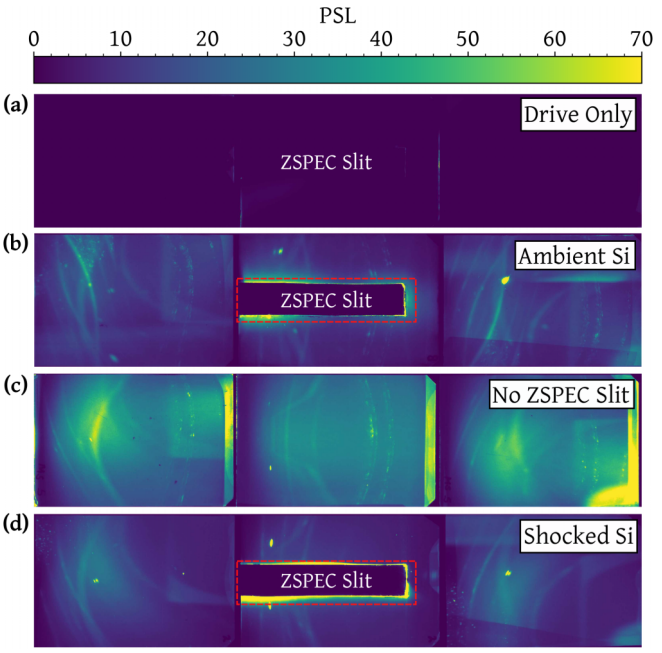

FIG. 8. Comparison of raw PXRDIP data for (a) drive only s30966, (b) ambient Si s30968, (c) s33539, which used an Ag pinhole and removed the ZSPEC access slit, and (d) s30967. The only contamination from the x-ray lasers is highlighted as a red dashed box around the ZSPEC slit in (d). This area is therefore excluded in future analysis. The higher signal level in s30968, and s33539 compared to s30967, is a result of a reflection off a Cu filter placed at the bottom of the PXRDIP box.

Subsequent analysis, therefore, utilizes s30970 as the background reference.

The scattering for the background s30970 and shocked s30967 shown in Figs. 9(a) and 9(b), respectively, is obtained by accounting for the filtering (12.5 μm Cu and 25 μm kapton), incident solid angle, polarization $[(1+\cos^2 2\theta)/2]$ and the attenuation of the scattered x-rays. The background subtracted shocked signal is shown in Fig. 9(c). Contamination at the edge of the IPs means a full integration in ϕ-space cannot be performed. The partial-ϕ integration region, highlighted in gray, therefore focuses on the IP center, and excludes the 2θ regions around the Ta Bragg peaks. The resultant liquid scattering signal is shown in blue in Fig. 9(d). The 12.5 μm Cu and 25 μm kapton filters used for the PXRDIP IPs have a 20% thickness uncertainty. Propagating this error through the background removal process results in the purple and olive plots shown in (d). The intensity error of each signal is given by the standard deviation from the mean signal along the ϕ integration. As we did not record to high-k, their absolute signal intensity is not applicable and they are normalized to their broad liquid scattering peak around 45°. This process demonstrates the effect that filter uncertainties have on the overall shape of the liquid scattering feature. The total liquid scattering signal uncertainty, as shown in Fig. 3(a), therefore encapsulates the region highlighted in gray.

APPENDIX C: VISAR ANALYSIS

Impedance matching techniques are used to infer the average shock speed through the silicon sample, D_{Si}. The total shock time through both the CH ablator and the Si sample

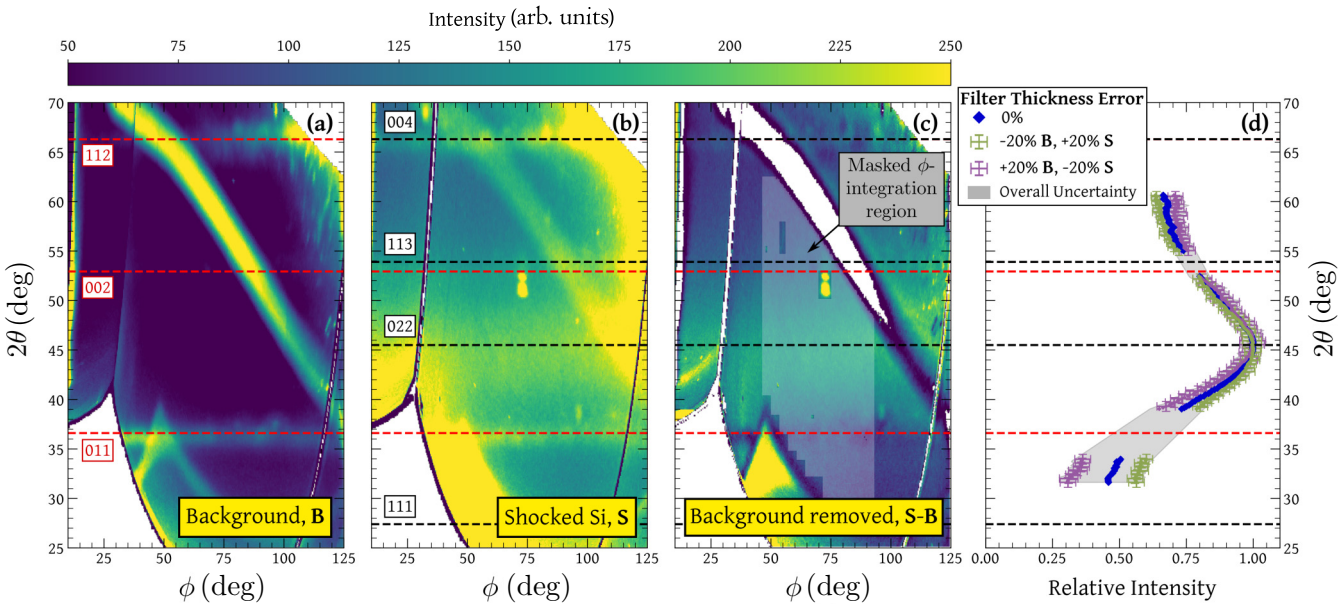

FIG. 9. (a) and (b) The warped, intensity-corrected signals at the sample position for background s30970 and shocked silicon s30967, respectively. The superimposed red and black dashed horizontal lines are the calibrated 2θ Bragg diffraction peaks of the Ta pinhole and the expected ambient silicon peaks, respectively. (c) Shocked Si scattering after background removal. Artifacts from this removal process are seen at the edges of the image plates. The region selected for ϕ-integration is highlighted in gray. (d) Shown in blue is the partial-ϕ integration of (c) to obtain the liquid scattering signal in 2θ. The purple and green lines show the effect that filter thickness uncertainties have on the inferred liquid shape. The overall signal uncertainty is taken over the gray shaded region.

is $t = t_{\mathrm{SBO}} - t_{\mathrm{drive}}$, where t_{SBO} and t_{drive} are the measured shock-breakout (SBO) and laser driver timings. These timings are listed in Table I, and an example of the VISAR diagnostic for s30967 is shown in Fig. 10. This total time can be related to the shock speeds in the Si and CH via

$$t = \frac{h_{\mathrm{Si}}}{D_{\mathrm{Si}}} + \frac{h_{\mathrm{CH}}}{D_{\mathrm{CH}}}, \tag{C1}$$

where h is the thickness of each material.

Silicon is opaque to the VISAR laser, meaning a direct measurement of particle velocity, U, cannot be obtained on each shot. The particle velocity in the shocked silicon is therefore inferred as [27]

$$D_{\mathrm{Si}} = 10.3(\pm 0.1) + 1.8(\pm 0.1)[U - 4.95], \tag{C2}$$

which is valid for $4 < U\ (\mathrm{km/s}) < 6.5$ and is based on the explosively driven data collected by Pavlovski in Ref. [42]. The corresponding linear relationship used for the CH ablator is [69]

$$D_{\mathrm{CH}} = 21.029(\pm 0.057) + 1.305(\pm 0.015)[U - 14.038]. \tag{C3}$$

As detailed in Fig. 11, these equations are used alongside the Rankine-Hugoniot relations, which are derived from the conservation of mass, momentum, and energy across a shock front, to infer the postshock P-ρ state,

$$P = P_0 + \rho_0 U_s U_p, \quad \rho = \frac{\rho_0 U_s}{U_s - U_p}, \tag{C4}$$

where $P_0 = 0\,\mathrm{GPa}$ and $\rho_0 = 2.329\,\mathrm{g/cm^3}$ are the preshock conditions. The silicon shock speed, pressure, and density for each shock-compressed experiment are listed in Table II.

APPENDIX D: HELIOS SIMULATIONS

Using the t_{SBO} measured with the VISAR diagnostic and by scaling the drive laser profile, HELIOS 1D simulations were produced for each shot using SESAME-EOS [57]. An example of the mass density through the target is shown in Fig. 12(a). The simulations emphasize the nonuniformity of the conditions within the silicon during the x-ray scattering

TABLE II. Comparison of the inferred plasma conditions for each shot using Rankine-Hugoniot relations on the left, and the Si mass-averaged conditions from HELIOS simulations during the scattering event on the right.

Shot	D_{Si} (km/s)	P (GPa)	ρ (g/cm^3)
	VISAR Transit Time		
30964	11.4 ± 0.3	146 ± 9	4.54 ± 0.07
30967	9.5 ± 0.2	101 ± 6	4.43 ± 0.08
33538	11.7 ± 0.3	155 ± 10	4.56 ± 0.07
33541	12.4 ± 0.2	178 ± 10	4.60 ± 0.07
	HELIOS Simulations		
30964	10.9 ± 0.2	70 ± 7	3.3 ± 0.2
30967	9.4 ± 0.1	48 ± 4	3.2 ± 0.1
33538	11.6 ± 0.2	81 ± 10	3.3 ± 0.2
33541	12.0 ± 0.2	82 ± 10	3.2 ± 0.2

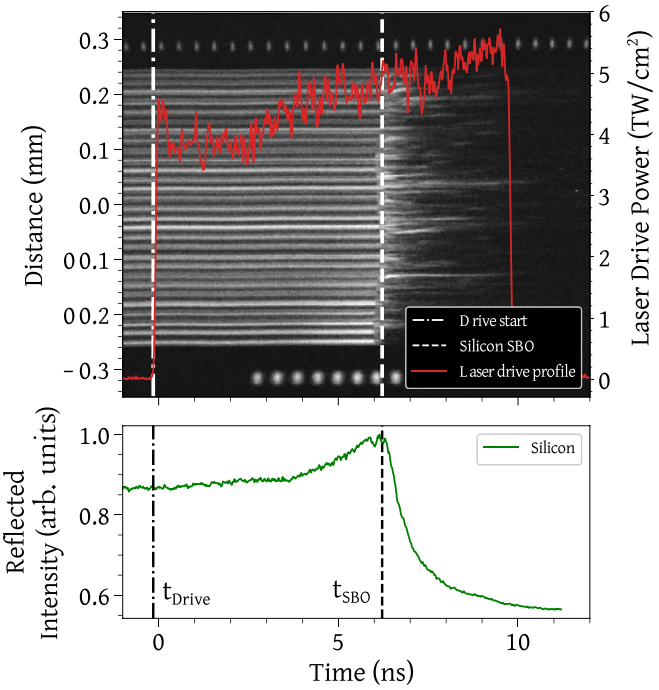

FIG. 10. Raw VISAR data from s30967. The fringes are reflected from the rear of the 51-μm-thick Si sample. Superimposed in red is the laser drive power. The integrated VISAR intensity is projected underneath. The time of shock-breakout, t_{SBO}, is determined as the point at which there is a sharp gradient decline in reflected VISAR signal.

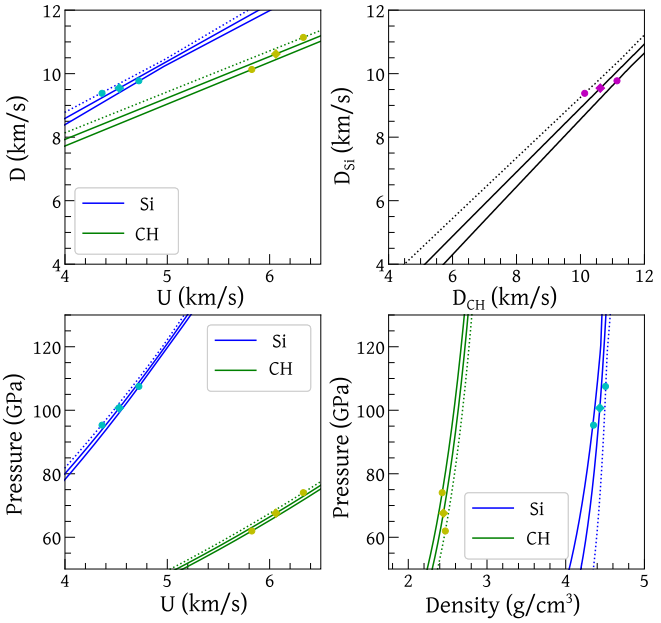

FIG. 11. Impedance matching CH and Si shock conditions, using Eqs. (C2)–(C4), to find (shown in the upper right quadrant) the linear relationship between D_{CH} and D_{Si}. The statistical errors arising from the CH and Si model uncertainties are shown throughout as fainter green and blue lines, respectively. The appropriate shock speed for each material (highlighted as a magenta diamond) is found by substituting the D_{CH}-D_{Si} relation into Eq. (C1). The corresponding 1σ errors due to both model and experimental uncertainties are shown as magenta circles. This information is carried through the remaining plots to find the corresponding P-ρ space for CH and Si.

event, which is highlighted in orange. The simulated shock speed through the silicon was determined by tracking the mass density gradient. An example of this shock tracking is shown as a thick red line in Fig. 12(a).

The simulated mass-averaged plasma conditions, $\langle X\rangle_m$ (where X is a plasma parameter), within the silicon during the x-ray probe were calculated as the mass-weighted average in space and averaged over the probe duration in time [70]. This is determined as

$$\langle X\rangle_m(t) = \frac{\sum_i V_i(t)\rho_i(t)X_i(t)}{\sum_i V_i(t)\rho_i(t)}, \tag{D1}$$

$$\langle X\rangle_m \equiv \langle\langle X\rangle_m(t)\rangle_t = \frac{\sum_{j_{\min}}^{j_{\max}} \langle X\rangle_m(t_j)t_j}{\Delta t_{\mathrm{xray}}}, \tag{D2}$$

where $V_i(t)$ is the volume in the ith cell at time t. The inferred P-ρ states for each shot are listed in Table II. These mass-averaged values are compared to the overall parameter distributions during the x-ray scattering event in Fig. 12. In the pre-SBO data, the sharp peaks corresponding to the low-density region indicate the presence of ambient silicon.

APPENDIX E: MARKOV-CHAIN MONTE CARLO ANALYSIS

MCMC is a robust method for exploring complex multiparameter spaces to overcome the challenge of inverse problem instability, which implies that the same measured experimental data can be fitted equally well by very different conditions. Given a specific set of parameters, $\Psi(\rho, T, Z)$, the multicomponent scattering spectra (MCSS) code [48] is used to produce a theoretical diffraction signal, $I_{\mathrm{fit}}(k)$. As discussed in the main paper, the scaling parameter γ for the experimentally measured liquid diffraction signal, $I_{\mathrm{liq}}(k)$, cannot be obtained experimentally. Instead we scale the experimental signal to the simulated fit using

$$\frac{I_{\mathrm{liq}}(k)}{\gamma} \equiv I_{\mathrm{scal}}(k) = I_{\mathrm{liq}}(k) \times \Gamma \frac{I_{\mathrm{fit}}^{\max}}{I_{\mathrm{liq}}^{\max}}, \tag{E1}$$

where Γ is a free random Gaussian scalar with a standard deviation equal to the noise of the raw data, and $I_{\mathrm{fit}}^{\max}$ and $I_{\mathrm{liq}}^{\max}$ are the peak values in the MCSS fit and raw x-ray scattering data, respectively.

The MCMC process then calculates the likelihood of these parameters producing the given scaled x-ray scattering spectrum, $I_{\mathrm{scal}}(k)$, as [30]

$$P(\Psi|I_{\mathrm{scal}}(k)) = \frac{P(I_{\mathrm{scal}}(k)|\Psi)P(\Psi)}{P(I_{\mathrm{scal}}(k))}, \tag{E2}$$

where $P(\Psi)$ is the prior distribution of possible parameters, $P(I_{\mathrm{scal}}(k))$ is the marginal likelihood of the observed data over all possible parameters, and the forward model likelihood, $P(I_{\mathrm{scal}}(k)|\Psi)$, is as described previously.

Model sensitivities for producing synthetic x-ray scattering signals using MCSS are shown in Fig. 13. This demonstrates how the dominant contributor to the synthetic scattering signal is the chosen ion-ion interaction potential, $V_{ii}(k)$. The

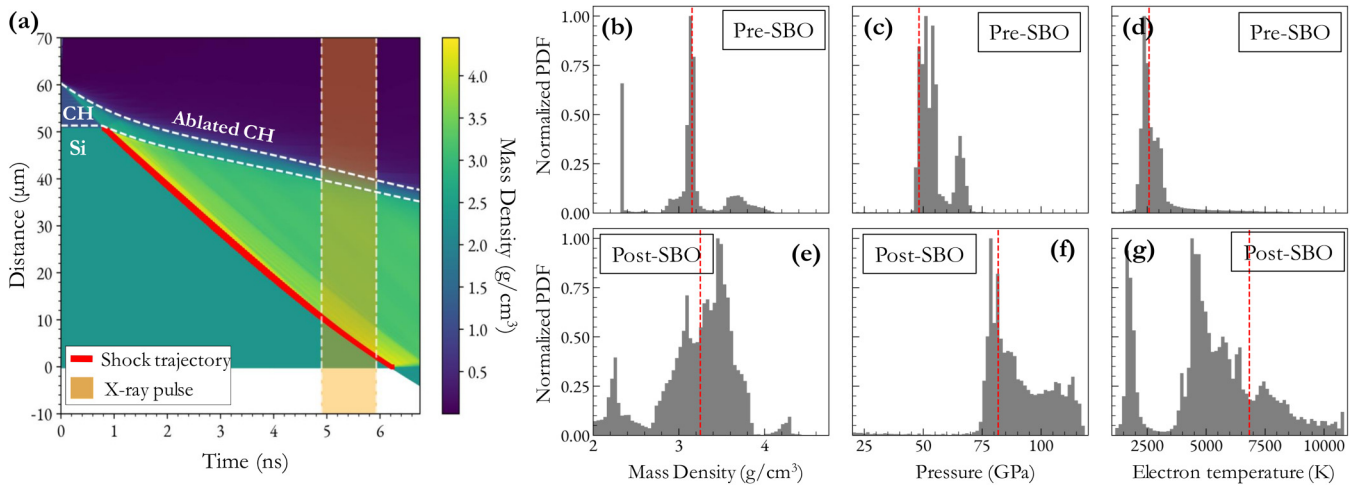

FIG. 12. (a) Eulerian HELIOS 1D simulation, produced by scaling the drive laser profile to match the measured t_{SBO}, for s30967. The silicon shock trajectory is shown as a thick red line, and the timing of the x-ray laser pulse is highlighted in orange. The subsequent histograms show the normalized probability distribution functions (PDFs) of the silicon conditions during the x-ray scattering event as predicted by the HELIOS simulations. The vertical red dashed lines are their respective mass-averaged values, $\langle X\rangle_m$. Panels (b)–(d) show the density, pressure and T_e, respectively, for s30967, taken before shock-breakout. Panels (e)–(g) as above for s33538, taken after shock-breakout.

screening models, $q(k)$, cannot be differentiated within the measured experimental error. The potentials for each $V_{ii}(k)$ are given by

$$V_{ii}^{ec}(k) = \frac{\mathcal{K}}{k^2}, \tag{E3}$$

where $\mathcal{K} = -Z^2e^2/\epsilon_0$,

$$V_{ii}^{dh}(k) = \frac{\mathcal{K}}{\kappa_e^2 + k^2}, \tag{E4}$$

where κ_e is the inverse screening length, and

$$V_{ii}^{nh}(k) = \frac{i\mathcal{K}}{2k\kappa_e}\left[\psi^{(1)}\left(1 + i\frac{k}{\kappa_e}\right) - \psi^{(1)}\left(1 - i\frac{k}{\kappa_e}\right)\right], \tag{E5}$$

where $\psi^{(1)}(x)$ is a trigamma function. The inverse screening length is taken as

$$\kappa_e = \sqrt{\frac{n_e e^2}{k_B T_e \epsilon_0}\frac{\mathcal{F}_{-1/2}(\eta_e)}{\mathcal{F}_{1/2}(\eta_e)}}, \tag{E6}$$

where $\mathcal{F}_j$ denotes the complete Fermi-Dirac integral of order j, and η_e is the dimensionless chemical potential of the free electrons,

$$\eta_e = \mathcal{F}_{1/2}^{-1}\left[\frac{n_e\hbar^3}{2}\left(\frac{2\pi}{m_e k_B T_e}\right)^{3/2}\right]. \tag{E7}$$

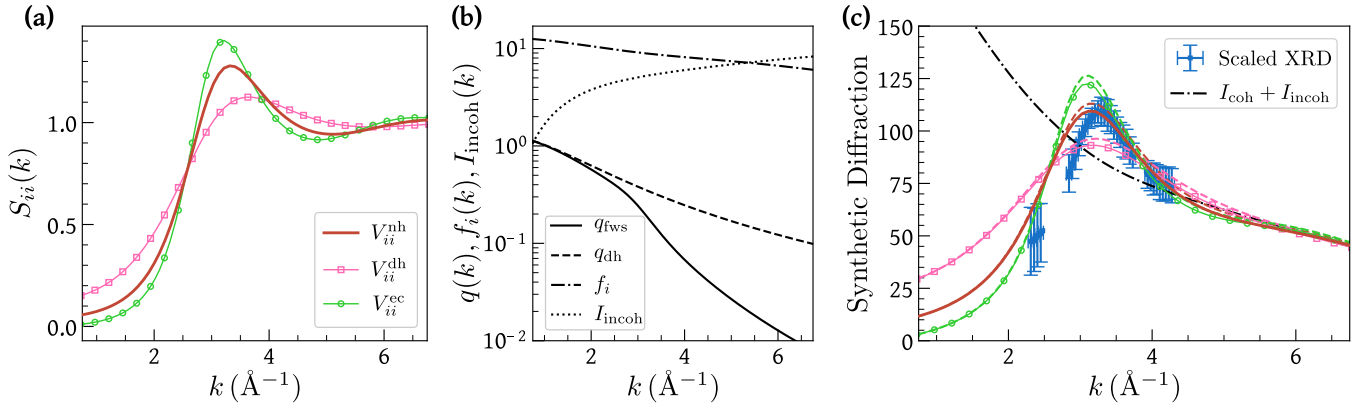

FIG. 13. (a) Ion-ion structure factors, $S_{ii}(k)$, for each $V_{ii}(k)$ using the mean parameters $\langle\Psi\rangle_{\mathrm{NH}}$ as shown in Fig. 3(a) ($\rho = 4.6\,\mathrm{g/cm^3}$, $Z = 1.3$, $T = 5300\,\mathrm{K}$). (b) Comparison of the tabulated incoherent scattering signal I_{incoh} [47], the bound electron form factor, $f(k)$, and the screening cloud, $q(k)$, produced with DH and FW models using $\langle\Psi\rangle_{\mathrm{NH}}$. (c) The synthetic diffraction signals produced with each $V_{ii}(k)$, $q(k)$, $f(k)$, and I_{incoh}, as shown in (a) and (b), compared to the scaled experimental scattering signal. For this representative plot, the scaling parameter, Γ, from Eq. (E1) was chosen using the NH I_{fit} (solid red curve).

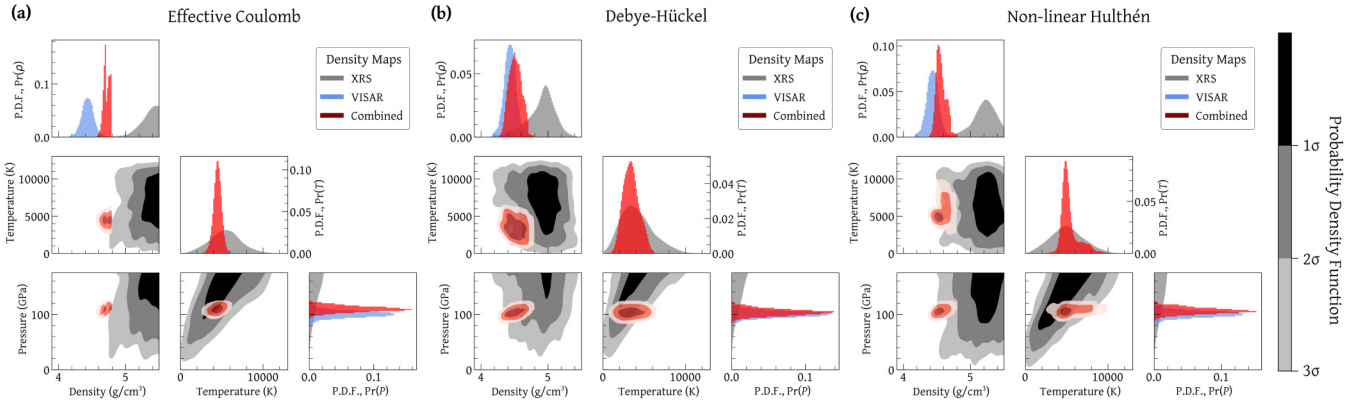

FIG. 14. Probability density functions for the liquid silicon density, pressure, and temperature state using the effective Coulomb (a), Debye-Hückel (b), and nonlinear Hulthén (c) $V_{ii}(k)$ models. As in Fig. 3(b), the lower quadrant plots compare the 1, 2, and 3σ parameter correlations for the MCMC converged x-ray scattering analysis (gray heat maps) and the combined density functions (red heat maps). The diagonal histograms show the probability densities for each parameter. The VISAR distributions are added in blue for density and pressure.

The converged shock-compressed silicon conditions using the effective Coulomb, Debye-Hückel, and nonlinear Hulthén models are shown in gray in Fig. 14.

From the convergence parameters, the total plasma pressure is determined using the "two-fluid" model described by Vorberger *et al.* [53,54],

$$P = \left(1 + \langle Z_i \rangle \frac{\mathcal{F}_{3/2}(\eta_e)}{n_e \Lambda_e^3/2}\right) n_i k_B T - n_i^2 \left.\frac{\partial f_e^{XC}}{\partial n_i}\right|_T - \frac{n_i^2}{4\pi^2}\frac{\partial}{\partial n_i}\left(\int_0^\infty \mathrm{d}k\, k^2\, \chi_{ee}(k,0)\left[V_{ei}^{\mathrm{eff}}(k)\right]^2\right)\Bigg|_T - 2\pi n_i^2 \int_0^\infty \mathrm{d}r\, r^2 \left[g_{ii}\left(r; V_{ii}^{\mathrm{eff}}(r)\right) - 1\right] \mathcal{V}_{ii}^{\mathrm{eff},P}(r), \quad \text{(E8)}$$

in which the effective ion-ion interaction potential for the evaluation of the excess ion pressure is defined as

$$\mathcal{V}_{ii}^{\mathrm{eff},P}(r) = \left(\frac{r}{3}\frac{\partial}{\partial r} - n_i \frac{\partial}{\partial n_i}\right) V_{ii}^{\mathrm{eff}}(r). \quad \text{(E9)}$$

In Eq. (E8), Λ_e is the thermal de Broglie wavelength of the free electrons. The first term is the sum of the ideal gas contributions from the ions and free electrons. In the second term, f_e^{XC} is the exchange-correlation contribution to the free energy (per particle) of the interacting electron gas [71]. The third term gives the contribution arising from electron-ion interactions in linear response, where the static electron density response function, $\chi_{ee}(k)$, is taken in the random phase approximation, and the local field correction, $G_{ee}(k)$, is determined using the effective static approximation [72]. The fourth term gives the excess pressure due to ionic correlations, where $g_{ii}(r; V_{ii}^{\mathrm{eff}}(r))$ is the pair distribution function of the ions [73] evaluated with a consistent effective ion-ion potential.

TABLE III. Comparison of the liquid silicon conditions within 1σ for the x-ray scattering MCMC convergence and the combined VISAR state using each ion-ion interaction potential.

$V_{ii}(k)$	ρ (g/cm^3)	P (GPa)	T (K)	$\bar{Z}$
MCMC convergence				
EC	5.5 ± 0.2	200 ± 60	6600 ± 2900	1.3 ± 0.3
DH	4.9 ± 0.2	250 ± 90	6900 ± 3000	3 ± 1
NH	5.2 ± 0.2	190 ± 60	6500 ± 3000	1.5 ± 0.4
MCMC and VISAR combined				
EC	4.72 ± 0.05	110 ± 5	4500 ± 500	1.01 ± 0.03
DH	4.51 ± 0.09	104 ± 6	3400 ± 1000	1.5 ± 0.1
NH	4.56 ± 0.07	106 ± 6	5300 ± 1100	1.26 ± 0.04

APPENDIX F: COMBINING VISAR AND MCMC ANALYSIS

As shown in Fig. 3, given the VISAR and MCMC P-ρ probability density functions, their subsequent joint probability is defined as

$$\mathrm{Pr}_j(\rho, P) = \frac{\mathrm{Pr}_m(\rho, P) \times \mathrm{Pr}_v(\rho, P)}{\sum_{\rho,P}\left[\mathrm{Pr}_m(\rho, P) \times \mathrm{Pr}_v(\rho, P)\right]}. \quad \text{(F1)}$$

These 2D combined density functions are shown as red heat maps in the lower left plots in Fig. 14. This formalism can be extended into multiparameter dimensions as the x-ray scattering analysis has dependencies beyond density and pressure. However, as VISAR provides no direct measurement of temperature, we must define its 3D density function such that $\mathrm{Pr}_v(\rho, P, T_i) \equiv \mathrm{Pr}_v(\rho, P, T_j)$, where $i \ (\neq j)$ describes a position along the temperature axis. By using Eq. (F1), the 2D phase space for pressure and temperature can subsequently be found as

$$\mathrm{Pr}_j(P, T) = \frac{\sum_\rho \mathrm{Pr}_j(\rho, P, T)}{\sum_{P,T}\left[\sum_\rho \mathrm{Pr}_j(\rho, P, T)\right]}. \quad \text{(F2)}$$

This process can be repeated in the ionization space.

The 1σ errors of each parameter's joint probability density function, i.e., $\mathrm{Pr}_j(\rho)$, are given in Table III. The phase diagrams in Fig. 4 detail the 1σ errors from $\mathrm{Pr}_j(\rho, P)$ and $\mathrm{Pr}_j(P, T)$, shown as the dark red contours in the lower left and central density maps in Fig. 14.

[1] A. Benuzzi-Mounaix, S. Mazevet, A. Ravasio, T. Vinci, A. Denoeud, M. Koenig, N. Amadou, E. Brambrink, F. Festa, A. Levy, M. Harmand, S. Brygoo, G. Huser, V. Recoules, J. Bouchet, G. Morard, F. Guyot, T. Resseguier, K. Myanishi, N. Ozaki, F. Dorchies, P. M. Gaudin, J. Leguay, O. Peyrusse, O. Henry, S. Raffestin, D. Pape, R. Smith, and R. Musella, Progress in warm dense matter study with applications to planetology, Phys. Scr. **T161**, 014060 (2014).

[2] T. G. Sharp and P. S. DeCarli, Shock effects in meteorites, Meteorites Early Solar Syst. II **943**, 653 (2006).

[3] F. Graziani, M. P. Desjarlais, R. Redmer, and S. B. Trickey, *Frontiers and Challenges in Warm Dense Matter* (Springer Science & Business, 2014), Vol. 96, p. vii.

[4] R. S. Craxton, K. S. Anderson, T. R. Boehly, V. N. Goncharov, D. R. Harding, J. P. Knauer, R. L. McCrory, P. W. McKenty, D. D. Meyerhofer, J. F. Myatt, A. J. Schmitt, J. D. Sethian, R. W. Short, S. Skupsky, W. Theobald, W. L. Kruer, K. Tanaka, R. Betti, T. J. B. Collins, J. A. Delettrez, S. X. Hu, J. A. Marozas, A. V. Maximov, D. T. Michel, P. B. Radha, S. P. Regan, T. C. Sangster, W. Seka, A. A. Solodov, J. M. Soures, C. Stoeckl, and J. D. Zuegel, Direct-drive inertial confinement fusion: A review, Phys. Plasmas **22**, 110501 (2015).

[5] S. X. Hu, L. A. Collins, T. R. Boehly, Y. H. Ding, P. B. Radha, V. N. Goncharov, V. V. Karasiev, G. W. Collins, S. P. Regan, and E. M. Campbell, A review on *ab initio* studies of static, transport, and optical properties of polystyrene under extreme conditions for inertial confinement fusion applications, Phys. Plasmas **25**, 056306 (2018).

[6] J. Badro, A. S. Côté, and J. P. Brodholt, A seismologically consistent compositional model of earth's core, Proc. Natl. Acad. Sci. (USA) **111**, 7542 (2014).

[7] G. A. de Wijs, G. Kresse, L. Vočadlo, D. Dobson, D. Alfe, M. J. Gillan, and G. D. Price, The viscosity of liquid iron at the physical conditions of the earth's core, Nature (London) **392**, 805 (1998).

[8] M. Landeau, A. Fournier, H.-C. Nataf, D. Cébron, and N. Schaeffer, Sustaining earth's magnetic dynamo, Nat. Rev. Earth Environ. **3**, 255 (2022).

[9] F. Soubiran, B. Militzer, K. P. Driver, and S. Zhang, Properties of hydrogen, helium, and silicon dioxide mixtures in giant planet interiors, Phys. Plasmas **24**, 041401 (2017).

[10] S. H. Glenzer, L. B. Fletcher, E. Galtier, B. Nagler, R. Alonso-Mori, B. Barbrel, S. B. Brown, D. A. Chapman, Z. Chen, C. B. Curry, F. Fiuza, E. Gamboa, M. Gauthier, D. O. Gericke, A. Gleason, S. Goede, E. Granados, P. Heimann, J. Kim, D. Kraus, M. J. MacDonald, A. J. Mackinnon, R. Mishra, A. Ravasio, C. Roedel, P. Sperling, W. Schumaker, Y. Y. Tsui, J. Vorberger, U. Zastrau, A. Fry, W. E. White, J. B. Hasting, and H. J. Lee, Matter under extreme conditions experiments at the linac coherent light source, J. Phys. B **49**, 092001 (2016).

[11] M. Koenig, A. Benuzzi-Mounaix, A. Ravasio, T. Vinci, N. Ozaki, S. Pape, D. Batani, G. Huser, T. Hall, D. Hicks, A. MacKinnon, P. Patel, H.-S. Park, T. Boehly, M. Borghesi, S. Kar, and L. Romagnani, Progress in the study of warm dense matter, Plasma Phys. Control. Fusion **47**, B441 (2005).

[12] K. Wünsch, J. Vorberger, G. Gregori, and D. O. Gericke, X-ray scattering as a probe for warm dense mixtures and high-pressure miscibility, Europhys. Lett. **94**, 25001 (2011).

[13] L. B. Fletcher, H. J. Lee, T. Döppner, E. Galtier, B. Nagler, P. Heimann, C. Fortmann, S. Le Pape, T. Ma, M. Millot, A. Pak, D. Turnbull, D. A. Chapman, D. O. Gericke, J. Vorberger, T. White, G. Gregori, M. Wei, B. Barbrel, R. W. Falcone, C.-C. Kao, H. Nuhn, J. Welch, U. Zastrau, P. Neumayer, J. B. Hastings, and S. H. Glenzer, Ultrabright x-ray laser scattering for dynamic warm dense matter physics, Nat. Photon. **9**, 274 (2015).

[14] E. E. McBride, A. Krygier, A. Ehnes, E. Galtier, M. Harmand, Z. Konôpková, H. J. Lee, H.-P. Liermann, B. Nagler, A. Pelka, M. Rödel, A. Schropp, R. F. Smith, C. Spindloe, D. Swift, F. Tavella, S. Toleikis, T. Tschentscher, J. S. Wark, and A. Higginbotham, Phase transition lowering in dynamically compressed silicon, Nat. Phys. **15**, 89 (2019).

[15] S. Brygoo, P. Loubeyre, M. Millot, J. R. Rygg, P. M. Celliers, J. H. Eggert, R. Jeanloz, and G. W. Collins, Evidence of hydrogen-helium immiscibility at jupiter-interior conditions, Nature (London) **593**, 517 (2021).

[16] H. Abu-Shawareb, R. Acree, P. Adams, J. Adams, B. Addis, R. Aden, P. Adrian, B. B. Afeyan, M. Aggleton, L. Aghaian *et al.*, Lawson criterion for ignition exceeded in an inertial fusion experiment, Phys. Rev. Lett. **129**, 075001 (2022).

[17] M. Bonitz, T. Dornheim, Z. A. Moldabekov, S. Zhang, P. Hamann, H. Kählert, A. Filinov, K. Ramakrishna, and J. Vorberger, *Ab initio* simulation of warm dense matter, Phys. Plasmas **27**, 042710 (2020).

[18] S. X. Hu, W. Theobald, P. B. Radha, J. L. Peebles, S. P. Regan, A. Nikroo, M. J. Bonino, D. R. Harding, V. N. Goncharov, N. Petta, T. C. Sangster, and E. M. Campbell, Mitigating laser-imprint effects in direct-drive inertial confinement fusion implosions with an above-critical-density foam layer, Phys. Plasmas **25**, 082710 (2018).

[19] P. Davis, T. Döppner, J. R. Rygg, C. Fortmann, L. Divol, A. Pak, L. Fletcher, A. Becker, B. Holst, P. Sperling, R. Redmer, M. P. Desjarlais, P. Celliers, G. W. Collins, O. L. Landen, R. W. Falcone, and S. H. Glenzer, X-ray scattering measurements of dissociation-induced metallization of dynamically compressed deuterium, Nat. Commun. **7**, 11189 (2016).

[20] D. Kraus, D. A. Chapman, A. L. Kritcher, R. A. Baggott, B. Bachmann, G. W. Collins, S. H. Glenzer, J. A. Hawreliak, D. H. Kalantar, O. L. Landen, T. Ma, S. Le Pape, J. Nilsen, D. C. Swift, P. Neumayer, R. W. Falcone, D. O. Gericke, and T. Döppner, X-ray scattering measurements on imploding ch spheres at the national ignition facility, Phys. Rev. E **94**, 011202(R) (2016).

[21] H. J. Lee, P. Neumayer, J. Castor, T. Döppner, R. W. Falcone, C. Fortmann, B. A. Hammel, A. L. Kritcher, O. L. Landen, R. W. Lee, D. D. Meyerhofer, D. H. Munro, R. Redmer, S. P. Regan, S. Weber, and S. H. Glenzer, X-ray thomson-scattering measurements of density and temperature in shock-compressed beryllium, Phys. Rev. Lett. **102**, 115001 (2009).

[22] S. P. Regan, K. Falk, G. Gregori, P. B. Radha, S. X. Hu, T. R. Boehly, B. J. B. Crowley, S. H. Glenzer, O. L. Landen, D. O. Gericke, T. Döppner, D. D. Meyerhofer, C. D. Murphy, T. C. Sangster, and J. Vorberger, Inelastic x-ray scattering from shocked liquid deuterium, Phys. Rev. Lett. **109**, 265003 (2012).

[23] F. Coppari, D. E. Fratanduono, M. Millot, R. G. Kraus, A. Lazicki, J. R. Rygg, R. F. Smith, and J. H. Eggert, X-ray diffraction measurements and pressure determination in nanosecond compression of solids up to 600 gpa, Phys. Rev. B **106**, 134105 (2022).

[24] X. Gong, D. N. Polsin, R. Paul, B. J. Henderson, J. H. Eggert, F. Coppari, R. F. Smith, J. R. Rygg, and G. W. Collins, X-ray diffraction of ramp-compressed silicon to 390 gpa, Phys. Rev. Lett. **130**, 076101 (2023).

[25] A. Lazicki, J. R. Rygg, F. Coppari, R. Smith, D. Fratanduono, R. G. Kraus, G. W. Collins, R. Briggs, D. G. Braun, D. C. Swift, and J. H. Eggert, X-ray diffraction of solid tin to 1.2 tpa, Phys. Rev. Lett. **115**, 075502 (2015).

[26] J. R. Rygg, J. H. Eggert, A. E. Lazicki, F. Coppari, J. A. Hawreliak, D. G. Hicks, R. F. Smith, C. M. Sorce, T. M. Uphaus, B. Yaakobi, and G. W. Collins, Powder diffraction from solids in the terapascal regime, Rev. Sci. Instrum. **83**, 113904 (2012).

[27] B. J. Henderson, M. C. Marshall, T. R. Boehly, R. Paul, C. A. McCoy, S. X. Hu, D. N. Polsin, L. E. Crandall, M. F. Huff, D. A. Chin, J. J. Ruby, X. Gong, D. E. Fratanduono, J. H. Eggert, J. R. Rygg, and G. W. Collins, Shock-compressed silicon: Hugoniot and sound speed up to 2100 gpa, Phys. Rev. B **103**, 094115 (2021).

[28] K. Falk, S. P. Regan, J. Vorberger, B. J. B. Crowley, S. H. Glenzer, S. X. Hu, C. D. Murphy, P. B. Radha, A. P. Jephcoat, J. S. Wark, D. O. Gericke, and G. Gregori, Comparison between x-ray scattering and velocity-interferometry measurements from shocked liquid deuterium, Phys. Rev. E **87**, 043112 (2013).

[29] J. Clérouin, N. Desbiens, V. Dubois, and P. Arnault, Bayesian inference of x-ray diffraction spectra from warm dense matter with the one-component-plasma model, Phys. Rev. E **94**, 061202(R) (2016).

[30] M. Kasim, T. P. Galligan, J. Topp-Mugglestone, G. Gregori, and S. M. Vinko, Inverse problem instabilities in large-scale modeling of matter in extreme conditions, Phys. Plasmas **26**, 112706 (2019).

[31] E. J. Davies, P. J. Carter, S. Root, R. G. Kraus, D. K. Spaulding, S. T. Stewart, and S. B. Jacobsen, Silicate melting and vaporization during rocky planet formation, J. Geophys. Res.: Planets **125**, e2019JE006227 (2020).

[32] K. Hirose, G. Morard, R. Sinmyo, K. Umemoto, J. Hernlund, G. Helffrich, and S. Labrosse, Crystallization of silicon dioxide and compositional evolution of the earth's core, Nature (London) **543**, 99 (2017).

[33] M. J. Edwards, J. D. Lindl, B. K. Spears, S. V. Weber, L. J. Atherton, D. L. Bleuel, D. K. Bradley, D. A. Callahan, C. J. Cerjan, D. Clark, G. W. Collins, J. E. Fair, R. J. Fortner, S. H. Glenzer, S. W. Haan, B. A. Hammel, A. V. Hamza, S. P. Hatchett, N. Izumi, B. Jacoby, O. S. Jones, J. A. Koch, B. J. Kozioziemski, O. L. Landen, R. Lerche, B. J. MacGowan, A. J. MacKinnon, E. R. Mapoles, M. M. Marinak, M. Moran, E. I. Moses, D. H. Munro, D. H. Schneider, S. M. Sepke, D. A. Shaughnessy, P. T. Springer, R. Tommasini, L. Bernstein, W. Stoeffl, R. Betti, T. R. Boehly, T. C. Sangster, V. Y. Glebov, P. W. McKenty, S. P. Regan, D. H. Edgell, J. P. Knauer, C. Stoeckl, D. R. Harding, S. Batha, G. Grim, H. W. Herrmann, G. Kyrala, M. Wilke, D. C. Wilson, J. Frenje, R. Petrasso, K. Moreno, H. Huang, K. C. Chen, E. Giraldez, J. D. Kilkenny, M. Mauldin, N. Hein, M. Hoppe, A. Nikroo, and R. J. Leeper, The experimental plan for cryogenic layered target implosions on the national ignition facility—the inertial confinement approach to fusion, Phys. Plasma **18**, 051003 (2011).

[34] G. Huser, N. Ozaki, P. Colin-Lalu, V. Recoules, T. Sano, Y. Sakawa, K. Miyanishi, and R. Kodama, Hugoniot equation of state of si-doped glow discharge polymer and scaling to other plastic ablators, Phys. Plasmas **25**, 052706 (2018).

[35] G. Fiksel, S. X. Hu, V. A. Goncharov, D. D. Meyerhofer, T. C. Sangster, V. A. Smalyuk, B. Yaakobi, M. J. Bonino, and R. Jungquist, Experimental reduction of laser imprinting and rayleigh–taylor growth in spherically compressed, medium-z-doped plastic targets, Phys. Plasmas **19**, 062704 (2012).

[36] S. X. Hu, G. Fiksel, V. N. Goncharov, S. Skupsky, D. D. Meyerhofer, and V. A. Smalyuk, Mitigating laser imprint in direct-drive inertial confinement fusion implosions with high-z dopants, Phys. Rev. Lett. **108**, 195003 (2012).

[37] J. R. Rygg, R. F. Smith, A. E. Lazicki, D. G. Braun, D. E. Fratanduono, R. G. Kraus, J. M. McNaney, D. C. Swift, C. E. Wehrenberg, F. Coppari, M. F. Ahmed, M. A. Barrios, K. J. M. Blobaum, G. W. Collins, A. L. Cook, P. Di Nicola, E. G. Dzenitis, S. Gonzales, B. F. Heidl, M. Hohenberger, A. House, N. Izumi, D. H. Kalantar, S. F. Khan, T. R. Kohut, C. Kumar, N. D. Masters, D. N. Polsin, S. P. Regan, C. A. Smith, R. M. Vignes, M. A. Wall, J. Ward, J. S. Wark, T. L. Zobrist, A. Arsenlis, and J. H. Eggert, X-ray diffraction at the national ignition facility, Rev. Sci. Instrum. **91**, 043902 (2020).

[38] D. D. Meyerhofer, J. Bromage, C. Dorrer, J. H. Kelly, B. E. Kruschwitz, S. J. Loucks, R. L. McCrory, S. F. B. Morse, J. F. Myatt, P. M. Nilson, J. Qiao, T. C. Sangster, C. Stoeckl, L. J. Waxer, and J. D. Zuegel, Performance of and initial results from the omega ep laser system, J. Phys.: Conf. Ser. **244**, 032010 (2010).

[39] F. Coppari, R. F. Smith, D. B. Thorn, J. R. Rygg, D. A. Liedahl, R. G. Kraus, A. Lazicki, M. Millot, and J. H. Eggert, Optimized x-ray sources for x-ray diffraction measurements at the omega laser facility, Rev. Sci. Instrum. **90**, 125113 (2019).

[40] A. L. Meadowcroft, C. D. Bentley, and E. N. Stott, Evaluation of the sensitivity and fading characteristics of an image plate system for x-ray diagnostics, Rev. Sci. Instrum. **79**, 113102 (2008).

[41] P. M. Celliers and M. Millot, Imaging velocity interferometer system for any reflector (visar) diagnostics for high energy density sciences, Rev. Sci. Instrum. **94**, 011101 (2023).

[42] M. N. Pavlovskii, Formation of metallic modifications of germanium and silicon under shock loading, Sov. Phys. Solid State **9**, 2514 (1968).

[43] S. J. Turneaure, S. M. Sharma, and Y. M. Gupta, Nanosecond melting and recrystallization in shock-compressed silicon, Phys. Rev. Lett. **121**, 135701 (2018).

[44] J. W. E. Drewitt, Liquid structure under extreme conditions: high-pressure x-ray diffraction studies, J. Phys.: Condens. Matter **33**, 503004 (2021).

[45] S. Singh, A. L. Coleman, S. Zhang, F. Coppari, M. G. Gorman, R. F. Smith, J. H. Eggert, R. Briggs, and D. E. Fratanduono, Quantitative analysis of diffraction by liquids using a pink-spectrum x-ray source, J. Synch. Radiat. **29**, 1033 (2022).

[46] J. Chihara, Interaction of photons with plasmas and liquid metals-photoabsorption and scattering, J. Phys.: Condens. Matter **12**, 231 (2000).

[47] J. H. Hubbell, W. J. Veigele, E. A. Briggs, R. T. Brown, D. T. Cromer, and R. J. Howerton, Atomic form factors, incoherent scattering functions, and photon scattering cross sections, J. Phys. Chem. Ref. Data **4**, 471 (1975).

[48] D. A. Chapman, User guide and theoretical basis for the multi-component scattering spectra (MCSS) thomson scattering analysis code, AWE Report 12/17 (AWE, 2017).

[49] H. Poole, R. Epstein, D. Cao, I. Golovkin, T. Walton, S. X. Hu, M. Kasim, S. M. Vinko, J. R. Rygg, V. N. Goncharov, G. Gregori, and S. P. Regan, A case study of using x-ray thomson scattering to diagnose the in-flight plasma conditions of DT cryogenic implosions, Phys. Plasmas **29**, 072703 (2022).

[50] P. Debye, and E. Hückel, On the theory of electrolytes. I. Freezing point depression and related phenomena, Phys. Z. **24**, 185 (1923).

[51] Y. P. Varshni, Eigenenergies and oscillator strengths for the hulthén potential, Phys. Rev. A **41**, 4682 (1990).

[52] D. A. Chapman, J. Vorberger, L. B. Fletcher, R. A. Baggott, L. Divol, T. Döppner, R. W. Falcone, S. H. Glenzer, G. Gregori, T. M. Guymer, A. L. Kritcher, O. L. Landen, T. Ma, A. E. Pak, and D. O. Gericke, Observation of finite-wavelength screening in high-energy-density matter, Nat. Commun. **6**, 6839 (2015).

[53] W. Ebeling, H. Reinholz, and G. Röpke, Hydrogen, helium and lithium plasmas at high pressures, Eur. Phys. J.: Spec. Top. **229**, 3403 (2020).

[54] J. Vorberger, D. O. Gericke, and W.-D. Kraeft, The equation of state for hydrogen at high densities, High Energy Density Phys. **9**, 448 (2013).

[55] M. Schörner, M. Bethkenhagen, T. Döppner, D. Kraus, L. B. Fletcher, S. H. Glenzer, and R. Redmer, X-ray thomson scattering spectra from density functional theory molecular dynamics simulations based on a modified chihara formula, Phys. Rev. E **107**, 065207 (2023).

[56] B. B. L. Witte, M. Shihab, S. H. Glenzer, and R. Redmer, Ab initio simulations of the dynamic ion structure factor of warm dense lithium, Phys. Rev. B **95**, 144105 (2017).

[57] B. I. Bennett, J. D. Johnson, G. I. Kerley, and G. T. Rood, Recent developments in the sesame equation-of-state library, Los Alamos National Laboratory, Los Alamos, NM, Technical Report LA-7130, 5150206 (1978).

[58] R. M. More, K. H. Warren, D. A. Young, and G. B. Zimmerman, A new quotidian equation of state (qeos) for hot dense matter, Phys. Fluids **31**, 3059 (1988).

[59] J. J. MacFarlane, I. E. Golovkin, and P. R. Woodruff, Helios-cr–a 1-d radiation-magnetohydrodynamics code with inline atomic kinetics modeling, J. Quant. Spectrosc. Radiat. Transf. **99**, 381 (2006).

[60] S. X. Hu, B. Militzer, L. A. Collins, K. P. Driver, and J. D. Kress, First-principles prediction of the softening of the silicon shock hugoniot curve, Phys. Rev. B **94**, 094109 (2016).

[61] R. Paul, S. X. Hu, and V. V. Karasiev, Crystalline phase transitions and vibrational spectra of silicon up to multiterapascal pressures, Phys. Rev. B **100**, 144101 (2019).

[62] T. Goto, T. Sato, and Y. Syono, Reduction of shear strength and phase-transition in shock-loaded silicon, Jpn. J. Appl. Phys. **21**, L369 (1982).

[63] W. H. Gust and E. B. Royce, Axial yield strengths and two successive phase transition stresses for crystalline silicon, J. Appl. Phys. **42**, 1897 (1971).

[64] R. Paul, S. X. Hu, and V. V. Karasiev, Anharmonic and anomalous trends in the high-pressure phase diagram of silicon, Phys. Rev. Lett. **122**, 125701 (2019).

[65] R. Paul (private Communication).

[66] O. Strickson and E. Artacho, Ab initio calculation of the shock hugoniot of bulk silicon, Phys. Rev. B **93**, 094107 (2016).

[67] A. Pak, G. Gregori, J. Knight, K. Campbell, D. Price, B. Hammel, O. L. Landen, and S. H. Glenzer, X-ray line measurements with high efficiency bragg crystals, Rev. Sci. Instrum. **75**, 3747 (2004).

[68] A. Pelka, G. Gregori, D. O. Gericke, J. Vorberger, S. H. Glenzer, M. M. Gunther, K. Harres, R. Heathcote, A. L. Kritcher, N. L. Kugland, B. Li, M. Makita, J. Mithen, D. Neely, C. Niemann, A. Otten, D. Riley, G. Schaumann, M. Schollmeier, A. Tauschwitz, and M. Roth, Ultrafast melting of carbon induced by intense proton beams, Phys. Rev. Lett. **105**, 265701 (2010).

[69] M. A. Barrios, D. G. Hicks, T. R. Boehly, D. E. Fratanduono, J. H. Eggert, P. M. Celliers, G. W. Collins, and D. D. Meyerhofer, High-precision measurements of the equation of state of hydrocarbons at 1–10 mbar using laser-driven shock waves, Phys. Plasmas **17**, 056307 (2010).

[70] D. A. Chapman, D. Kraus, A. L. Kritcher, B. Bachmann, G. W. Collins, R. W. Falcone, J. A. Gaffney, D. O. Gericke, S. H. Glenzer, T. M. Guymer, J. A. Hawreliak, O. L. Landen, S. Le Pape, T. Ma, P. Neumayer, J. Nilsen, A. Pak, R. Redmer, D. C. Swift, J. Vorberger, and T. Döppner, Simulating x-ray thomson scattering signals from high-density, millimetre-scale plasmas at the national ignition facility, Phys. Plasmas **21**, 082709 (2014).

[71] S. Groth, T. Dornheim, T. Sjostrom, F. D. Malone, W. M. C. Foulkes, and M. Bonitz, Ab initio exchange-correlation free energy of the uniform electron gas at warm dense matter conditions, Phys. Rev. Lett. **119**, 135001 (2017).

[72] T. Dornheim, Z. A. Moldabekov, and P. Tolias, Analytical representation of the local field correction of the uniform electron gas within the effective static approximation, Phys. Rev. B **103**, 165102 (2021).

[73] J.-P. Hansen and I. R. McDonald, *Theory of Simple Liquids: With Applications to Soft Matter* (Academic, 2013), p. 106, Chap. 4.